RESEARCH ARTICLE

*National Science Open*
2: 20220037, 2023
https://doi.org/10.1360/nso/20220037

Chemistry

Special Topic: Chemistry Boosts Carbon Neutrality

# Defect and interface control on graphitic carbon nitrides/upconversion nanocrystals for enhanced solar hydrogen production

Xiaochun Gao[1,2,#], Nailiang Yang[3,4,#], Jin Feng[5], Jiayan Liao[6], Shaoqi Hou[1], Xiaoguang Ma[2], Dawei Su[1,*], Xingxing Yu[1], Ziqing Yang[2], Javad Safaei[1], Dan Wang[3,4,*] & Guoxiu Wang[1,*]

[1]*Centre for Clean Energy Technology, Faculty of Science, University of Technology Sydney, Broadway, NSW 2007, Australia;*
[2]*School of Physics and Optoelectronic Engineering, Ludong University, Yantai 264000, China;*
[3]*State Key Laboratory of Biochemical Engineering, Institute of Process Engineering, Chinese Academy of Sciences, Beijing 100190, China;*
[4]*University of Chinese Academy of Sciences, Beijing 100049, China;*
[5]*School of Chemistry and Chemical Engineering, Qufu Normal University, Qufu 273165, China;*
[6]*Institute for Biomedical Materials and Devices (IBMD), Faculty of Science, University of Technology Sydney, Ultimo, NSW 2007, Australia*

#Contributed equally to this work.
*Corresponding authors (emails: Dawei.Su@uts.edu.au (Dawei Su); danwang@ipe.ac.cn (Dan Wang); Guoxiu.Wang@uts.edu.au (Guoxiu Wang))

Received 22 June 2022; Revised 10 October 2022; Accepted 10 October 2022; Published online 22 December 2022

**Abstract:** The effective utilization of solar energy for hydrogen production requires an abundant supply of thermodynamically active photo-electrons; however, the photocatalysts are generally impeded by insufficient light absorption and fast photocarrier recombination. Here, we report a multiple-regulated strategy to capture photons and boost photocarrier dynamics by developing a broadband photocatalyst composed of defect engineered g-$C_3N_4$ (DCN) and upconversion $NaYF_4$:$Yb^{3+}$,$Tm^{3+}$ (NYF) nanocrystals. Through a precise defect engineering, the S dopants and C vacancies jointly render DCN with defect states to effectively extend the visible light absorption to 590 nm and boost photocarrier separation via a moderate electron-trapping ability, thus facilitating the subsequent re-absorption and utilization of upconverted photons/electrons. Importantly, we found a promoted interfacial charge polarization between DCN and NYF has also been achieved mainly due to Y-N interaction, which further favors the upconverted excited energy transfer from NYF onto DCN as verified both theoretically and experimentally. With a 3D architecture, the NYF@DCN catalyst exhibits a superior solar $H_2$ evolution rate among the reported upconversion-based system, which is 19.3 and 1.5 fold higher than bulk material and DCN, respectively. This work provides an innovative strategy to boost solar utilization by using defect engineering and building up interaction between hetero-materials.

**Keywords:** broadband, precise defect engineering, atomic interaction, solar hydrogen production

## INTRODUCTION

Solar-to-hydrogen conversion has been regarded as a promising and sustainable strategy to alleviate the steadily worsening energy crisis and environmental issues caused by fossil fuels [1]. To maximize solar utilization, enormous efforts have been focused on exploiting highly efficient photocatalysts to produce abundant thermodynamically active photo-electrons by extending the light absorption from ultraviolet (UV)

to near-infrared (NIR) region and improving photocarrier separation efficiency [2]. Unfortunately, a single photocatalyst alone can hardly satisfy all the above requirements as the NIR-responsive bandgap is generally thought to lack photocatalytic activity or directly convert NIR solar energy into heat [3,4]. Fortunately, upconverison materials such as carbon quantum dots (CQDs) featuring capturing long-wavelength light to emitting short-wavelength light via surface traps and trivalent lanthanide-based lanthanides ($Ln^{3+}$) ion-doped $NaYF_4$ possessing lower vibrational energy (~360 $cm^{-1}$≈45 meV) to absorb NIR light and emit UV-visible (UV-vis) light via two or multi-photon absorption/energy conversion have attracted extensive research interest [5–8]. For the former, QDs suffer from chemical stability, hindering its further applications in photocatalytic activity. While for the latter, $Ln^{3+}$-ions such as $Er^{3+}$, $Tm^{3+}$ are frequently used as co-dopants with $Yb^{3+}$ to produce stable and efficient energy transfer in upconversion luminescence due to their ladder-like energy levels and long-lived intermediate excited states [9]. However, the realization of their photocatalytic activity largely relies on the electronic/optical properties of the core photocatalyst [10,11]. Despite great progress has been made toward these broadband photocatalytic system, the study on the interaction between the upconversion material and photocatalyst is rarely reported.

Exhibiting an excellent absorption of UV light, polymerized graphitic carbon nitride (g-$C_3N_4$) has recently become the hottest core photocatalyst particularly owing to the tailorable electronic structure via defect engineering [12]. Although most literature has emphasized the positive roles of defects such as extended light absorption and electrons buffering sites [13–15], their potential side effect of being recombination centers of surface photocarriers has been neglected. Thus, precise defect control on g-$C_3N_4$ is necessary, otherwise the over-strong electron-trapping ability of defect states would conversely lower the light utilization from both "external" sun and "inner" upconverted materials [16]. Moreover, considering the larger electronic negativity of C and N atoms, it might form an interaction between g-$C_3N_4$ and metallic atoms in upconversion materials. This interaction may promote the charge transport at interface, but the deeper understanding at the atomic level is still missing.

In this case, we firstly introduce defect engineering on g-$C_3N_4$, and assemble it with upconversion composition, forming three-dimensional (3D) architecture. Both theoretical calculations and experiments were performed to understand how the S dopants and C vacancies induced defect states in defective g-$C_3N_4$ (DCN), extending its visible light response to 590 nm. For the first time, we realize a precise defect control on DCN by endowing its defect states with a moderate electron-trapping ability, and thus an efficient photocarrier separation is acquired, which is beneficial for the subsequent utilization of upconverted photons. Furthermore, by integrating the upconversion $NaYF_4$:$Yb^{3+}$,$Tm^{3+}$ (NYF) nanocrystals onto DCN, we successfully obtain a broadband photocatalyst (NYF@DCN) that can capture UV, visible, and NIR photons. Interestingly, we found a promoted interfacial charge polarization between DCN and NYF has also been achieved mainly due to Y-N interaction, which has been verified from both theoretical and experimental analysis. Thus, compared to the unmodified bulk g-$C_3N_4$ (BCN), DCN is more favorable to accept the migrated energy from NYF nanocrystals via both enhanced fluorescence re-absorption and excited energy transfer process due to the precise defect controls and Y-N atomic interaction, respectively. As a result, the photocatalytic performance of the as-developed broadband photocatalyst has been enhanced by 19.3 times compared with bulk g-$C_3N_4$, which ranks the top among the reported upconversion-based photocatalysis system.

## RESULTS AND DISCUSSION

As depicted in Figure 1A, a series of NYF-*x*@DCN catalysts (where *x* represents the mass percentage of NYF nanocrystals) were prepared by the pyrolysis of ethylene glycol (EG)-assisted self-assembled melamine-cyanurate (MCA-EG) and subsequent thermal treatment with NYF. To preserve the 3D framework of DCN, the size and annealing condition of the precursors were prudently studied (Figure S1, see details in the Supplementary Information). The growth of hexagonal MCA-EG nanocolumns was restricted to a size of ~1 μm in length and 200 nm in width (Figure 1B). While sulfur acts as another morphology protecting agent

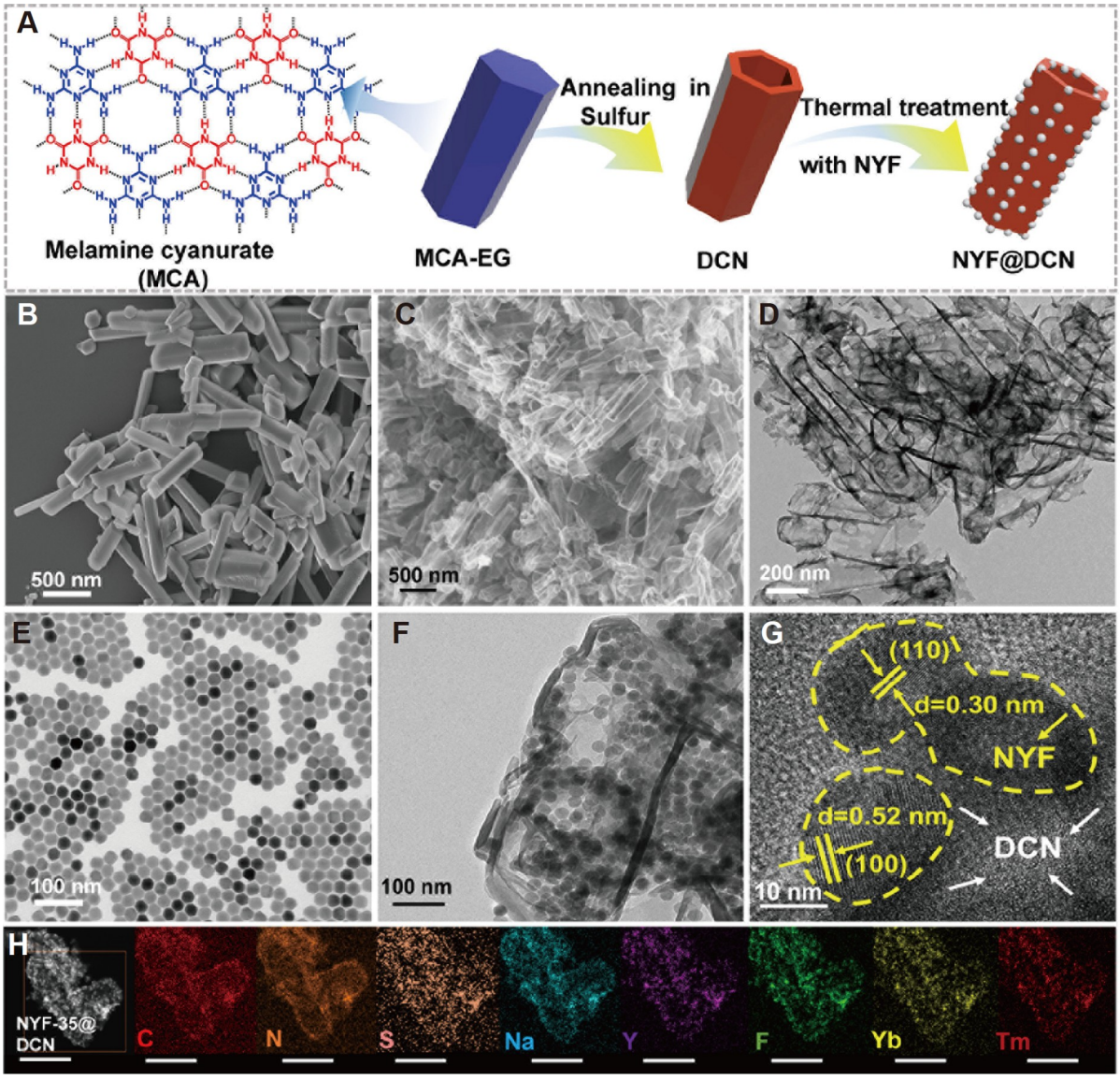


**Figure 1** (A) Schematic illustration for the fabrication of NYF@DCN. SEM images of (B) MCA-EG and (C) DCN. Transmission electron microscopy (TEM) images of (D) DCN, (E) NYF, (F) NYF-35@DCN. (G) High-resolution transmission electron microscopy (HRTEM) image of NYF-35@DCN. (H) High-magnification scanning transmission electron microscopy image with the corresponding elemental mapping of C, N, S, Na, Y, F, Yb, and Tm for NYF-35@DCN (scale bar: 500 nm).

during the air thermal exfoliation process, which is confirmed by the well-established hexagonal nanocolumns of DCN (Figure 1C and 1D) and the split nanosheets/nanoflakes of its counterparts (Figure S1B–S1D). The NYF upconversion nanocrystals (25 nm) also demonstrate a uniform hexagonal shape and robust thermal stability as their morphology and crystallinity are well preserved even after the post-thermal treatment (Figure 1E–G, Figure S2) [17]. Benefiting from the 3D scaffold, the NYF nanocrystals (≤35 wt%) are uniformly distributed on the surface of DCN nanocolumns (Figure 1F, Figure S3). While DCN exhibits non-obvious lattice fringe along (002) orientation due to the weakened (002) crystalline plane, suggesting an intensive thermal exfoliation process (Figure 1G, Figure S2). Moreover, DCN and NYF@DCN present a hierarchical meso-macroporous structure with higher surface area and larger pore volume, compared to the non-modified BCN (Figures S1E and S1F, and S4, Table S1). For DCN, the S-dopants and successful coupling with NYF are also confirmed by the elemental mapping result (Figure 1H).

With a doping-level of 0.55%, S atoms substitute the two-coordinated N atoms in the basic tri-s-triazine ring to form C–S–C bond in DCN (Figure 2A, Figure S5, and Table S2) [18]. While the C vacancies are verified by the weakened *g* signal intensity at ~2.0042 that originates from the unpaired electrons in C atoms as reflected from the electron paramagnetic resonance (EPR) spectrum (Figure 2B) [19]. Moreover, the pronounced double peaks around ~3200 $cm^{-1}$ are assigned to the primary amine group (Figure S6) [19,20], which further demonstrats the presence of two-coordinated C vacancies in DCN. As a result, compared with BCN, DCN shows an increased and decreased concentration of C–N–H and $–C_3N$, respectively (Figure S5c, Table S3). As a result, the S dopants and C vacancies-derived defects not only change the original chemical environment (Figure S5B–S5D) but also alter the electronic structure and optical property of g-$C_3N_4$. We propose a calculated DCN model with the atomic C:N:S ratio of 34:46:1 based on the experimental surface element ratio (C:N:S ratio of 39:58:1, Table S2, insert in Figure 2C). The negative formation energies of −3.82 and −4.25 eV for g-$C_3N_4$ with S-dopant (CN*s*) and C-vacancy (CN*c*) further indicate that S dopants and C vacancies are energetically presented in two- and three-coordinated N sites, respectively (Figure S7). Compared to BCN, DCN shows a narrower bandgap as reflected by the density of states (DOSs) (Figure 2C, Figure S8). More importantly, for DCN, significant states of N 2p and C 2p around the Fermi level are presented, which implies the generation of defect states and improved electrical conductivity (Figure 2C). The existence of defect states in DCN is further experimentally confirmed by the absorption shoulder around 500 nm and the Urbach tail [15] as reflected in the UV-vis diffusion reflectance absorption spectra (Figure 2D). Based on the Kubelk-Munk function [21], DCN shows a 0.21 eV lower bandgap of 2.60 eV than BCN, and the position of defect states is calculated to be 2.10 eV above the VB, suggesting the utilization of photons excited with much lower energy and an enhanced visible absorption up to 590 nm (Figure S9). After coupling with NYF, the NYF-35@DCN exhibits a distinctive absorption band around 980 nm, assigning to $^2F_{7/2}\rightarrow{}^2F_{5/2}$ transition of the dopant $Yb^{3+}$, which demonstrates its broadband light absorption property. Moreover, the photoluminescence spectra show that the hexagonal NYF nanocrystals can upconvert NIR energy into higher UV and visible light photons, corresponding to the transitions of $^1I_6\rightarrow{}^3F_4$ (345 nm), $^1D_2\rightarrow{}^3H_6$ (361 nm), $^1D_2\rightarrow{}^3F_4$ (451 nm), $^1G_4\rightarrow{}^3H_6$ (475 nm), $^1G_4\rightarrow{}^3F_4$ (646 nm) and $^3H_4\rightarrow{}^3H_6$ (800 nm), respectively (Figure 2E, Figure S10) [22]. However, the NYF-35@DCN hybrid exhibits negligible UV emissions (Figure S10) and the dramatically reduced intensity ratio of the blue emissions (451, 475 nm) to yellow emission (650 nm) from 10.9 to 2.4 (Figure 2E). These weakened emissions are covered in the light absorption region of DCN, thus they can be theoretically re-absorbed by DCN via the photon transfer

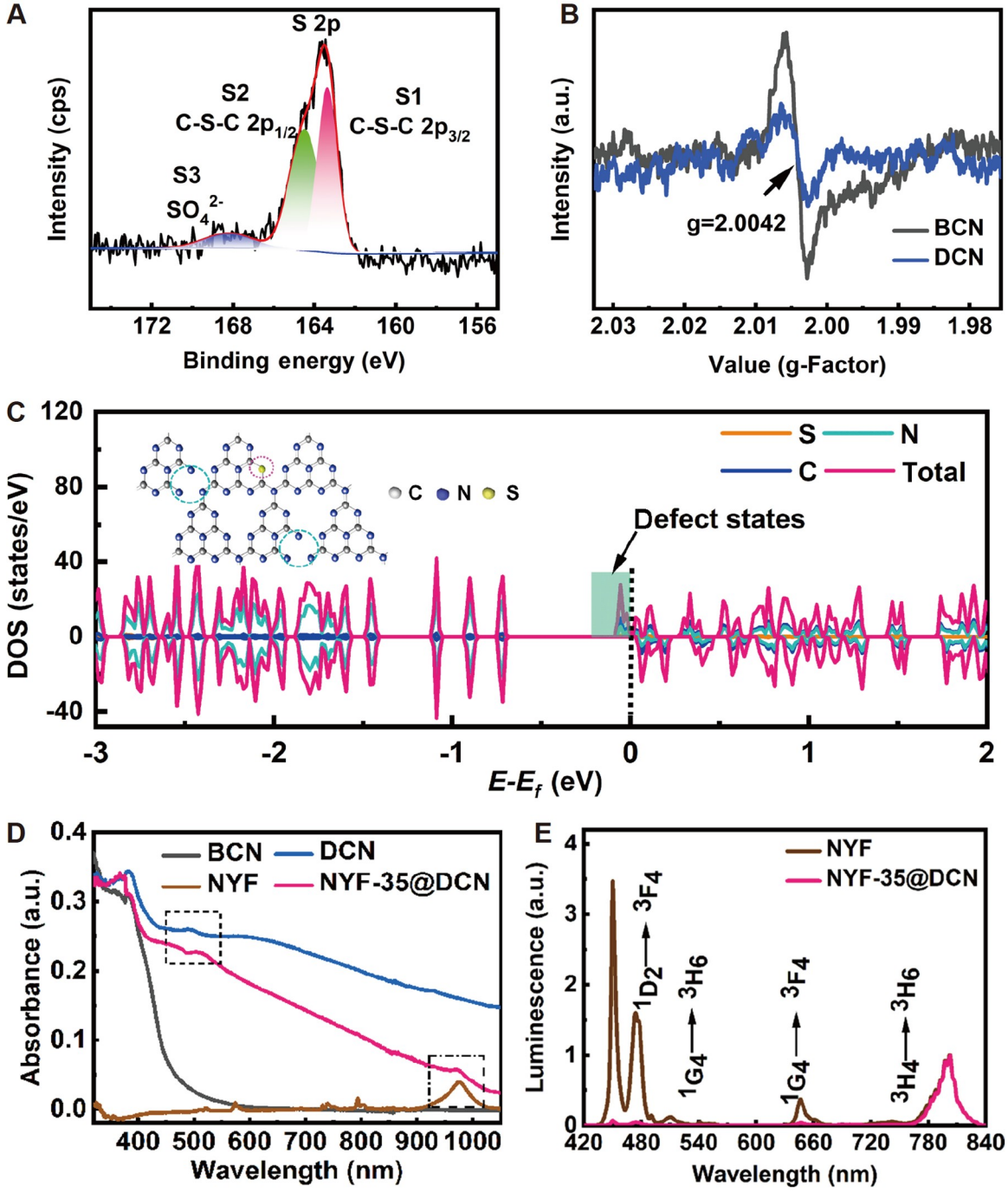


**Figure 2** (A) Core-level XPS spectrum of S 2p for DCN. (B) EPR spectra of BCN and DCN. (C) DOSs of DCN (insert: proposed structure of DCN; the Fermi level is defined as 0 eV). (D) UV-vis diffusion reflectance absorption spectra of BCN, DCN, NYF, and NYF-35@DCN (selected area: defect states and NIR absorption). (E) Upconversion photoluminescence spectra of NYF and NYF-35@DCN.

process.

Employing a typical three-electrode cell system, the 1 μm thick photoelectrode was back-illuminated under a chopped simulated solar light (Figure S11). Figure 3A shows the transient photocurrents of BCN, DCN, and

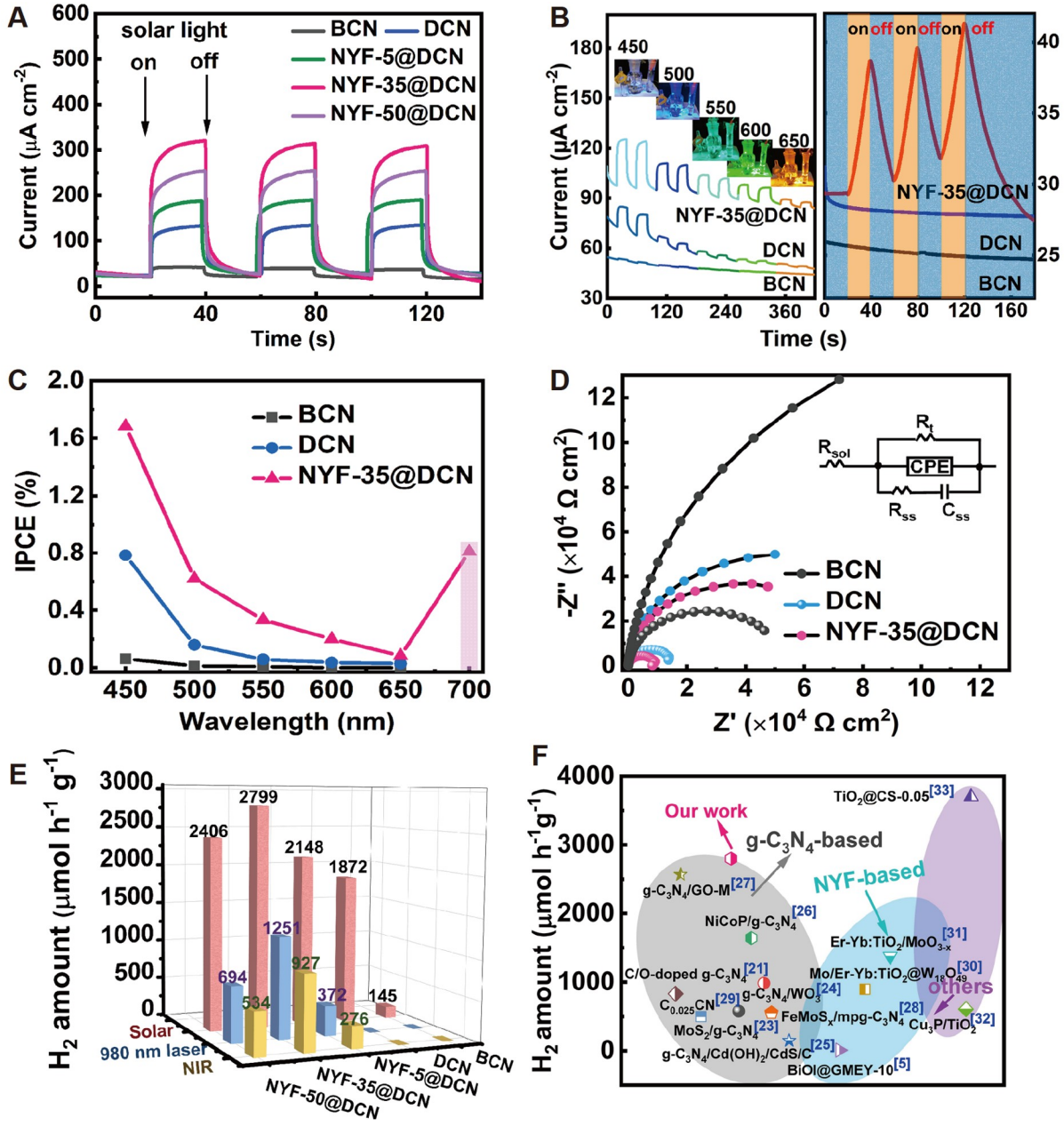


**Figure 3** (A) Transient photocurrent responses at 0.2 V vs. AgCl/Ag electrode. (B) Transient photocurrent responses at longer wavelengths of 450, 500, 550, 600, 650 (left) and 98–0 nm (right) for BCN, DCN, and NYF-35@DCN. (C) IPCE curves of BCN, DCN, and NYF-35@DCN. (D) EIS Nyquist plots (insert: equivalent circuit). (E) $H_2$ evolution rate for BCN, DCN, and NYF@DCN hybrids under solar and 980 nm laser irradiation. (F) Comparison of solar $H_2$ evolution rate of NYF-35@DCN with representative reported photocatalysts.

NYF@DCN catalysts at 0.2 V (vs. Ag/AgCl). Compared to BCN with a rectangular curve of photocurrent, DCN shows a steadily increasing photocurrent which further demonstrates the success of defect engineering, which is consistent with PL (conduction band) result (Figure S12). This originates from the more complex competition between electron accumulation and charge recombination within the DCN film due to the additional energy levels that provide more photo-excited electrons from VB (valence band) and accept more

migrated electrons from CB (conduction band) to the fluorine-doped tin oxide (FTO) substrate. Specifically, NYF-35@DCN, NYF-50@DCN, NYF-5@DCN, DCN, and BCN, in decreasing order, deliver a photocurrent of 301, 234, 167, 112, and 7 μA $cm^{-2}$, respectively. This implies an optimized mass loading of NYF nanocrystals is necessary to obtain the highest photocarriers separation efficiency. Notably, NYF-35@DCN also displays the highest photocurrents even at a wavelength longer than its bandgap excitation ($\lambda$=476 nm), i.e., 16.01 μA $cm^{-2}$ at 500 nm, 12.55 μA $cm^{-2}$ at 550 nm, and 8.15 μA $cm^{-2}$ at 650 nm (Figure 3B, left). This enhanced visible light utilization can be ascribed to the reduced photon-excited energy (<2.60 eV) caused by the defect states (Figure S9). The contribution of upconversion NYF nanocrystals is further verified by an obvious photocurrent of 8.01 μA for NYF-35@DCN with a 980 nm laser (Figure 3B, right). Compared to BCN and DCN, NYF-35@DCN shows an overwhelming superiority on incident photon-to-current efficiency (IPCE) over all wavelengths, demonstrating the boosted solar energy conversion after the multiple regulations on carbon nitrides (Figure 3C, Table S4). Electrochemical impedance spectroscopy (EIS) measurement shows NYF-35@DCN has the lowest charge transfer resistance ($R_{ct}$) of $7.67\times10^4$ Ω $cm^2$ (Figure 3D), which is lower than that of DCN ($8.77\times10^4$ Ω $cm^2$, Table S5). This is mainly due to its enhanced bulk electrical conductivity induced by defects in DCN and the lower intrinsic resistance of NYF. The reduced resistance is also reflected by the highest dark photocurrent as seen from the photovoltammograms (Figure S13). Moreover, under simulated solar irradiation, NYF-35@DCN also presents the lowest $R_{ct}$ value of $9.10\times10^3$ Ω $cm^2$, suggesting the superior photoelectrochemical property and significantly decreased transport obstacle for photocarriers (Table S6).

As a result, DCN displays an improved photocatalytic $H_2$ evolution rate of 1872 μmol $h^{-1}$ $g^{-1}$, which is 12.9 times higher than that of BCN, indicating the success of defect engineering (Figure 3E, Figure S14). To study whether the upconversion nanocrystals could boost the NIR energy utilization of DCN, the $H_2$ generation performance of all materials was evaluated under 980 nm laser with an intensity of ~15 mW $cm^{-2}$ (Figure S15). The negligible photocatalytic activity was witnessed for DCN and NYF. While the NYF-*x*@DCN exhibits significantly enhanced $H_2$ evolution rate up to 1251 μmol $h^{-1}$ $g^{-1}$ with an optimized NYF mass loading of 35%, which indicates the positive effect of upconversion coupling (Figure S14). To further evaluate the practical $H_2$ evolution, the hybrid materials were also irradiated under solar light whose light intensity at 980 nm is much lower than that of 980 nm laser. Compared to bare DCN, NYF-5@DCN, NYF-35@DCN, and NYF-5@DCN also achieve higher $H_2$ evolution rate of 2148, 2799, and 2406 μmol $h^{-1}$ $g^{-1}$ with the NYF-assocaited contribution of 276, 927, and 534 μmol $h^{-1}$ $g^{-1}$, respectively (Figure 3E). This enhanced performance of NYF-x@DCN confirms the energy transfer between NYF and DCN can occur even under solar irradiation. Moreover, we also performed a controlled experiment using the defective stacked g-$C_3N_4$ nanosheets with S dopants and C vacancies (abbreviated as DCN-HS, Figure S16) as the supporting matrix for NYF to study the stereo structure effect. The hybrid (NYF-35@DCN-HS) shows an inferior hydrogen evolution rate and photocurrent of 2239 μmol $h^{-1}$ $g^{-1}$ and 108.50 μA $cm^{-2}$ (Figure S17), indicating the indispensable role of 3D architecture toward solar light utilization. Furthermore, NYF-35@DCN exhibits superior apparent quantum efficiency (Figure S18) and robust stability against photocorrosion as evidenced by the continuous $H_2$ evolution without noticeable deterioration (Figure S19) and persistent scanning electron microscopy (SEM), Fourier transformed infrared spectroscopy (FT-IR) and X-ray diffraction (XRD) patterns after reaction (Figure S20). As an overview of the state-of-the-art, the solar $H_2$ evolution performance of NYF-35@DCN not only ranks the top among the g-$C_3N_4$ based photocatalysts but

also exceeds the upconversion particles-based and other traditional photocatalysts (Figure 3F, Table S7) [5,21,23–33].

In a control experiment, we explore the necessity of EG solvent and sulfur powder on final defect controls toward suppressed surface recombination. A series of defective g-$C_3N_4$ samples employing $H_2O$-assisted self-assembled melamine-cyanurate (MCA-$H_2O$), MCA-$H_2O$ and sulfur, and MCA-EG as precursors are denominated as DCN-H, DCN-HS, and DCN-E, respectively. As shown in Figure 4A, DCN shows a moderate increase of suface state capacitance ($C_{ss}$) of 3.15 μF $cm^{-2}$ compared to BCN (0.96 μF $cm^{-2}$) and DCN-E (4.52 μF $cm^{-2}$) under simulated solar light (Figure S21, Table S8) [34], indicating a limited increase of charge density in these surface states by buffering the photo-excited electrons from CB or the transited electrons from VB. To explore the strength of the electron-trapping, the pseudo-first-order rate constant ($k$) of surface photocarrier recombination is calculated using the following equation based on the decay profiles of the open-circuit potential (Figure 3F) [35]:

$$\left(V - V_{\text{light}}\right) / \left(V_{\text{dark}} - V_{\text{light}}\right) = 1 - \exp(-kt), \quad (1)$$

where $V$, $V_{\text{dark}}$, and $V_{\text{light}}$ are the open-circuit potential, in the dark and under light irradiation, respectively (Figure 4B). As a result, DCN presents the slowest decay kinetics (0.021 $s^{-1}$) compared to BCN (0.384 $s^{-1}$), DCN-H (0.036 $s^{-1}$), DCN-HS (0.067 $s^{-1}$), and DCN-E (0.045 $s^{-1}$). This means the suppressed recombination and prolonged lifetimes of surface photocarriers for DCN, implying the modest electron-trapping ability of defect sites via the synthetic controls using both EG and sulfur powder. In addition, the calculated $k$ of NYF-35@DCN is around 0.018 $s^{-1}$, which is slightly lower than that of DCN (Figure S22). The lower $k$ of hybrid material implies the improved photocarrier separation efficiency induced by the upconversion coupling, which is consistent with the PEC and photocatalytic performance (Figure 3A and 3E). Thus, our defect-engineered DCN greatly alleviates the recombination of surface photocarriers, guaranteeing an efficient supply of thermodynamically active electrons into the subsequent photocatalytic redox activity.

At this stage, it is critical to reveal the underlying energy migration of NYF@DCN for a deep understanding of the synergistic effect between upconversion and defect engineering toward solar $H_2$ evolution: (1) To provide direct evidence of photon transfer (PT) process, the transient photocurrent test was performed with a purpose-designed electrode in which BCN and DCN were pasted on the conductive side of FTO glass while NYF was pasted on the non-conductive side (Figure S23). Illuminating NYF with a 980 nm laser, NYF‖FTO‖DCN electrode shows a higher photocurrent (1.01 μA $cm^{-2}$) than NYF‖FTO‖BCN (0.17 μA $cm^{-2}$). This confirms that the defect engineered g-$C_3N_4$ is more favorable in harvesting the upconverted fluorescence. (2) Moreover, the time-resolved fluorescence decay curves recorded by a home-made scanning confocal microscope under a 980 nm pulsed laser [36,37] show that NYF-35@DCN exhibits a shorter lifetime of 179 μs than NYF of 255 μs at 451 nm (Figure S24). This indicates the upconverted energy can also be transferred via the non-radiative excited state energy transfer (ET) pathway from $Tm^{3+}$ $^1D_2$ excited state to CB/defect states of DCN [22,38,39]. Notably, the ET process can be further accelerated due to the interaction between DCN and NYF nanocrystals, which is demonstrated by the solid-state nuclear magnetic resonance spectra (ssNMR) measured under a cross-polarization magic angle spinning mode (CP-MAS). The CP-MAS $^{13}C$ NMR spectra show no obvious chemical shift change for both DCN and NYF-35@DCN, suggesting that the upconversion nanocrystals have no significant interference with C of tri-s-triazine unit (Figure S25). Notably, for the $^{15}N$ NMR spectra, we observe a peak multiplicity disappearance around 106.6

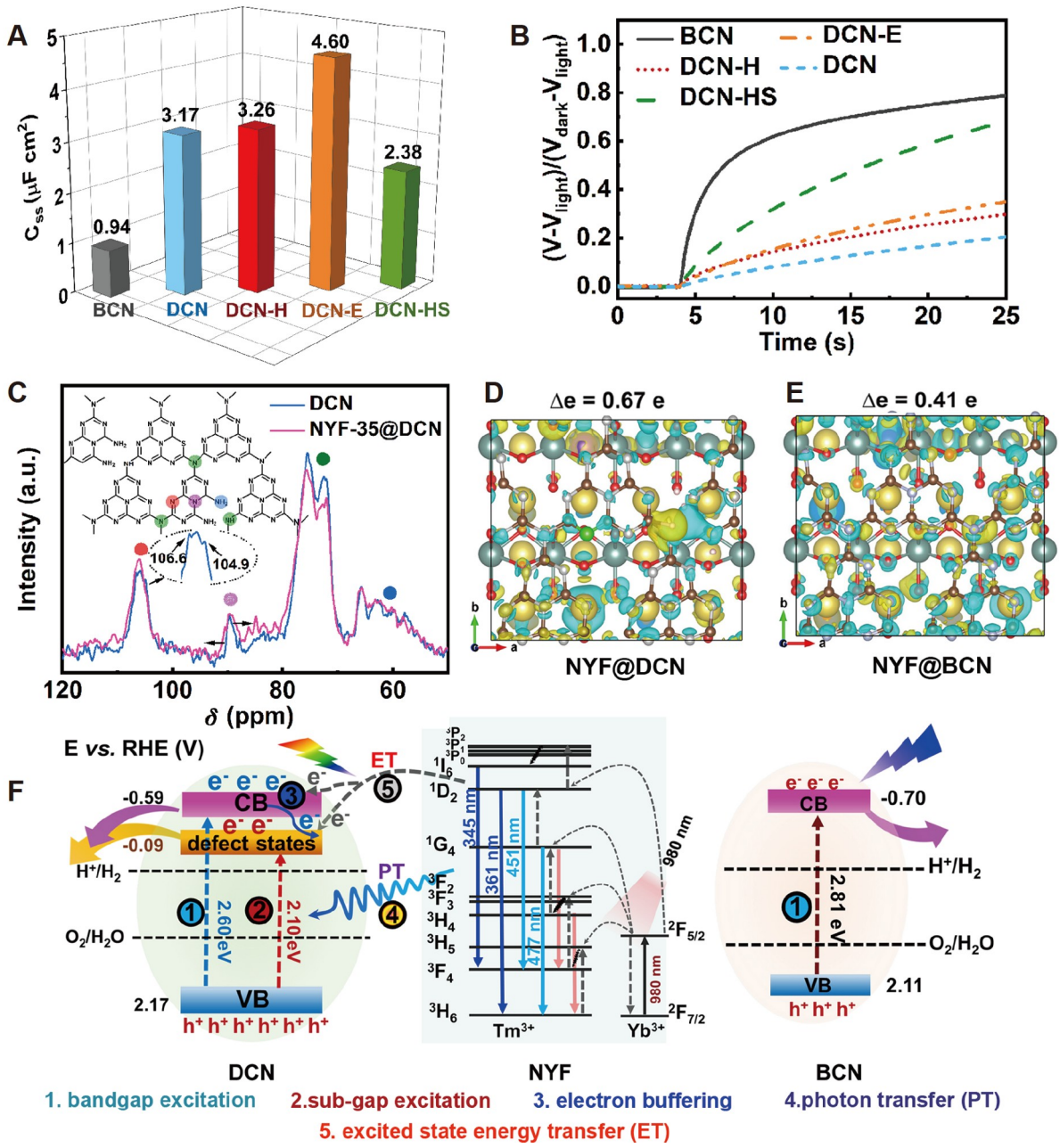


**Figure 4** (A) Comparison of $C_{ss}$ calculated from EIS data and (B) open-circuit potential decay curves of BCN, DCN, and other defective g-$C_3N_4$ samples. (C) CP-MAS $^{15}$N NMR spectra of DCN and NYF-35@DCN. Differential charge density between (D) NYF@DCN and (E) NYF@BCN (olive and cyan iso-surfaces represent the region of net electron accumulation and deficit; grey: C; brown: N; green: S; yellow: Na; dark grey: Y; red: F; blue: Yb; purple: Tm). (F) Proposed photocatalytic mechanism of NYF@DCN photocatalysts.

and 104.9 ppm for the intermediate N atom (red, 102.2–109.5 ppm, Figure 4C) after NYF coupling, which could be induced by their interactions with the cations in $NaYF_4$:$Yb^{3+}$,$Tm^{3+}$ that shield H atoms. In addition, the peak broadening for central N that is close to C vacancies (purple, 87.0–91.2 ppm) also indicates the interaction between DCN and NYF nanoparticles [40,41]. The XPS (X-ray photoelectron spectroscopy)

shows N shifts to lower binding energy while Y significantly shifts 0.5–0.6 eV to higher binding energy (Figure S26). Therefore, we draw a conclusion that there exists a Y-N interaction between DCN and NYF, where N atoms are mostly the intermediate N and defective central N. This enhanced interaction might be induced by the intimate contact after thermal treatment because the physically mixed counter (NYF-35@DCN-p) shows an inferior photocatalytic activity than NYF-35@DCN (Figure S27). Figure 4D and 4E shows the density functional theory (DFT)-based charge density difference diagrams and illustrates the stronger electronic interaction and polarization at the interface of NYF@DCN than NYF@BCN, as the net charge change is 0.67 e vs. 0.41 e. This suggests that the defects in DCN might also play a more favorable role in strengthening the composite affinity and dynamically facilitating the excited state ET process compared with the unmodified BCN. Therefore, defect engineered g-$C_3N_4$ is more favorable in accepting the photon energy from the upconverted energy from NYF via both PT and excited state ET pathway.

Based on the above analyses, we propose a schematic for the solar light harvesting and charge transfer process for NYF@DCN (Figure 4F). According to the calculated bandgap and defect states level (Figure S9), the band structures of BCN and DCN were drawn after measuring their CB positions at −0.70 and −0.59 V vs. reference hydrogen electrode (RHE), respectively (Figure S28). Under solar light irradiation, the electrons involved in hydrogen evolution are dominantly excited via the following five ways: (1) Under UV and visible light illumination with wavelength <476 nm, the electrons in the VB of DCN can be excited to the CB (−0.59 V) via a bandgap excitation, simultaneously leaving VB with positive holes to react with scavenger. (2) Due to the defect engineering on DCN, additional electrons will be excited to the defect states level (−0.09 V), which thermodynamically satisfies hydrogen evolution requirement via the sub-gap excitation, extending the visible light absorption region to 590 nm. (3) Acting as an electron buffering level, the defect states of DCN can accept the electrons from CB and work as electron reservoirs with a moderate electron-trapping ability, preventing their rapid recombination with holes in VB. (4) Under NIR light illumination ($\lambda$= 980 nm), the photons in NYF are excited to the long-lived $^2F_{5/2}$ level of $Yb^{3+}$ sensitizer and transfer to the activated levels of $^1I_6$, $^1D_2$, and $^1G_4$ of $Tm^{3+}$ activator [42]. The upconverted UV and blue emissions centering around 345, 361, 451, and 477 nm are subsequently released and act as a secondary light source to re-excite DCN with extra electrons in CB or defect states via a PT pathway. (5) While a proportion of excited electrons in $^1I_6$ and $^1D_2$ levels are transferred to DCN via a non-radiative excited state ET process. More importantly, this energy transfer can be further accelerated due to the Y-N interaction, and thus a facilitated charge transfer dynamic onto DCN is attained. Finally, due to the enhanced light-harvesting ability of DCN and enhanced electronic polarization at the interface of NYF@DCN, a fascinating synergetic effect between defect states and upconversion is achieved. This broadband photocatalyst with porous 3D architecture, intimate contact between nanocomponents, enhanced light absorption, and accelerated charge transfer process ultimately boosts a superior hydrogen evolution performance.

## CONCLUSION

In summary, we have successfully developed a broadband photocatalyst by coupling hexagonal $NaYF_4$:$Yb^{3+}$,$Tm^{3+}$ upconversion nanocrystals onto the surface of defect engineered g-$C_3N_4$ nanocolumns. Through a precise defect control, the S dopants and C vacancies jointly render DCN with defect states, which

are effective in both extending light absorbance from 441 to 590 nm and alleviating the photocarrier recombination via a narrower bandgap and moderate electron trapping ability. Moreover, the $Yb^{3+}$ and $Tm^{3+}$ cations further upconvert NIR light into UV-vis light to re-excite the electron-hole pairs in DCN or impart the excited electrons from $^1I_6$ and $^1D_2$ levels to CB/defect states of DCN, enabling NYF@DCN a full-solar-spectral photocatalyst for hydrogen production. Importantly, we revealed the promoted interfacial charge polarization between DCN and NYF mainly contributed by the Y-N interaction. Due to the moderate electron trapping ability of defects and Y-N interaction, DCN is more favorable to accept the upconverted energy transferred from NYF via both PT and excited state ET pathway. As a result, the NYF@DCN performs as a full-solar-spectral photocatalyst, which exhibits a superior $H_2$ evolution activity of 2799 μmol $h^{-1}$ $g^{-1}$, ranking the top among the g-$C_3N_4$ based photocatalysts and upconversion particles-based photocatalysts. This work provides an understanding on the interaction between metallic and non-metallic materials and presents an avenue to boost photocatalytic property via multiple regulations.

## Funding

D. Su would like to acknowledge the support by the Australia Research Council (ARC) through the ARC Discovery Early Career Researcher Award (DECRA DE170101009) and University of Technology Sydney (UTS), through the UTS Chancellor's Postdoctoral Research Fellowship project. G. Wang is grateful for the support provided by the ARC through the ARC DP200101249 project. J. Feng would like to thank the computational resources provided by the High-Performance Computing Center of Qufu Normal University. D. Wang would like to acknowledge the National Natural Science Foundation of China (21903048, 21971244, 51932001, 21931012, 21590795) and National Key R&D Program of China (2018YFA0703504, 2021YFB3802600).

## Author contributions

D.W. Su, D. Wang and G.X. Wang conceived the project, designed the experiments and co-supervised the research; X.C. Gao and N.L. Yang conducted the synthesis, characterization, and wrote the manuscript. J. Liao processed the data; J. Feng performed DFT calculations; J.Y. Liao perfomed the PL spectrum; S.Q. Hou, X.G. Ma, X.X. Yu, Z.Q. Yang, and J. Safaei edited the manuscript. All the authors discussed the results and participated in the preparation of the paper.

## Conflict of interest

The authors declare no conflict of interest.

## Supplementary information

The supporting information is available online at https://doi.org/10.1360/nso/20220037. The supporting materials are published as submitted, without typesetting or editing. The responsibility for scientific accuracy and content remains entirely with the authors.

## References

1 Rahman MZ, Edvinsson T, Gascon J. Hole utilization in solar hydrogen production. *Nat Rev Chem* 2022; **6**: 243–258.

2 Jin B, Cho Y, Park C, *et al.* A two-photon tandem black phosphorus quantum dot-sensitized $BiVO_4$ photoanode for solar water splitting. *Energy Environ Sci* 2022; **15**: 672–679.

3 Sang Y, Zhao Z, Zhao M, *et al.* From UV to near-infrared, $WS_2$ nanosheet: A novel photocatalyst for full solar light spectrum photodegradation. *Adv Mater* 2015; **27**: 363–369.

4 Kang W, Deng N, Ju J, *et al.* A review of recent developments in rechargeable lithium-sulfur batteries. *Nanoscale* 2016; **8**: 16541–16588.

5 Wang C, Du P, Luo L, *et al.* Utilizing upconversion emission to improve the photocatalytic performance of the BiOI microplate: A bifunctional platform for pollutant degradation and hydrogen production. *Ind Eng Chem Res* 2021; **60**: 16245–16257.

6 Li B, Hu Y, Shen Z, *et al.* Photocatalysis driven by near-infrared light: materials design and engineering for environmentally friendly photoreactions. *ACS EST Eng* 2021; **1**: 947–964.

7 Chilkalwar AA, Rayalu SS. Synergistic plasmonic and upconversion effect of the (Yb,Er)NYF-$TiO_2$/Au composite for photocatalytic hydrogen generation. *J Phys Chem C* 2018; **122**: 26307–26314.

8 Chen Y, Huang G, Gao Y, *et al.* Up-conversion fluorescent carbon quantum dots decorated covalent triazine frameworks as efficient metal-free photocatalyst for hydrogen evolution. *Int J Hydrogen Energy* 2022; **47**: 8739–8748.

9 Kumar A, Kumar A, Chand H, *et al*. Upconversion nanomaterials for photocatalytic applications. In: Thomas S, Upadhyay K, Tamrakar R K, *et al.*, eds. *Upconversion Nanophosphors*. Amsterdam: Elsevier, 2022. 391–406.

10 Li M, Yao W, Liu J, *et al.* Facile synthesis and screen printing of dual-mode luminescent $NaYF_4$:Er,Yb (Tm)/carbon dots for anti-counterfeiting applications. *J Mater Chem C* 2017; **5**: 6512–6520.

11 Jiang L, Zhou S, Yang J, *et al.* Near-infrared light responsive $TiO_2$ for efficient solar energy utilization. *Adv Funct Mater* 2022; **32**: 2108977.

12 Wang J, Yu Y, Cui J, *et al.* Defective g-$C_3N_4$/covalent organic framework van der Waals heterojunction toward highly efficient S-scheme $CO_2$ photoreduction. *Appl Catal B-Environ* 2022; **301**: 120814.

13 Chen Z, Fan TT, Yu X, *et al.* Gradual carbon doping of graphitic carbon nitride towards metal-free visible light photocatalytic hydrogen evolution. *J Mater Chem A* 2018; **6**: 15310–15319.

14 Niu P, Qiao M, Li Y, *et al.* Distinctive defects engineering in graphitic carbon nitride for greatly extended visible light photocatalytic hydrogen evolution. *Nano Energy* 2018; **44**: 73–81.

15 Ran J, Ma TY, Gao G, *et al.* Porous P-doped graphitic carbon nitride nanosheets for synergistically enhanced visible-light photocatalytic $H_2$ production. *Energy Environ Sci* 2015; **8**: 3708–3717.

16 Henderson MA, White JM, Uetsuka H, *et al.* Photochemical charge transfer and trapping at the interface between an organic adlayer and an oxide semiconductor. *J Am Chem Soc* 2003; **125**: 14974–14975.

17 Liu D, Xu X, Du Y, *et al.* Three-dimensional controlled growth of monodisperse sub-50 nm heterogeneous nanocrystals. *Nat Commun* 2016; **7**: 10254.

18 Liu G, Niu P, Sun C, *et al.* Unique electronic structure induced high photoreactivity of sulfur-doped graphitic $C_3N_4$. *J Am Chem Soc* 2010; **132**: 11642–11648.

19 Li Y, Ho W, Lv K, *et al.* Carbon vacancy-induced enhancement of the visible light-driven photocatalytic oxidation of NO over g-$C_3N_4$ nanosheets. *Appl Surf Sci* 2018; **430**: 380–389.

20 Chang F, Zhang J, Xie Y, *et al.* Fabrication, characterization, and photocatalytic performance of exfoliated g-$C_3N_4$-$TiO_2$ hybrids. *Appl Surf Sci* 2014; **311**: 574–581.

21 Gao X, Feng J, Su D, *et al. In-situ* exfoliation of porous carbon nitride nanosheets for enhanced hydrogen evolution. *Nano Energy* 2019; **59**: 598–609.

22 Tang Y, Di W, Zhai X, *et al.* NIR-responsive photocatalytic activity and mechanism of $NaYF_4$:Yb,Tm@$TiO_2$ core-shell nanoparticles. *ACS Catal* 2013; **3**: 405–412.

23 Yuan YJ, Shen Z, Wu S, *et al.* Liquid exfoliation of g-$C_3N_4$ nanosheets to construct 2D-2D $MoS_2$/g-$C_3N_4$ photocatalyst for enhanced photocatalytic $H_2$ production activity. *Appl Catal B-Environ* 2019; **246**: 120–128.

24 Fu J, Xu Q, Low J, *et al.* Ultrathin 2D/2D $WO_3$/g-$C_3N_4$ step-scheme $H_2$-production photocatalyst. *Appl Catal B-Environ* 2019; **243**: 556–565.

25 Aleksandrzak M, Baranowska D, Kedzierski T, *et al.* Superior synergy of g-$C_3N_4$/Cd compounds and Al-MOF-derived nanoporous carbon for photocatalytic hydrogen evolution. *Appl Catal B-Environ* 2019; **257**: 117906.

26 Bi L, Gao X, Zhang L, *et al.* Enhanced photocatalytic hydrogen evolution of NiCoP/g-$C_3$ $N_4$ with improved separation

efficiency and charge transfer efficiency. *ChemSusChem* 2018; **11**: 276–284.

27 Li W, Chu X, Wang F, *et al.* Enhanced cocatalyst-support interaction and promoted electron transfer of 3D porous g-$C_3N_4$/GO-M (Au, Pd, Pt) composite catalysts for hydrogen evolution. *Appl Catal B-Environ* 2021; **288**: 120034.

28 Wang B, Yan C, Xu G, *et al.* Highly efficient solar-driven photocatalytic hydrogen evolution with $FeMoS_x$/mpg-$C_3N_4$ heterostructure. *Chem Eng J* 2022; **427**: 131507.

29 Xiao M, Jiao Y, Luo B, *et al.* Understanding the roles of carbon in carbon/g-$C_3N_4$ based photocatalysts for $H_2$ evolution. *Nano Res* 2021; https://doi/org/10.1007/s12274-021-3897-7.

30 Shang J, Xu X, Liu K, *et al.* Obvious effect of molybdenum supporting on morphology and upconversion luminescence of Er-Yb:$TiO_2$ and improvement of $H_2$ generation for $W_{18}O_{49}$. *J Alloys Compd* 2019; **785**: 610–615.

31 Shang J, Xu X, Liu K, *et al.* LSPR-driven upconversion enhancement and photocatalytic $H_2$ evolution for Er-Yb:$TiO_2$/$MoO_{3-x}$ nano-semiconductor heterostructure. *Ceramics Int* 2019; **45**: 16625–16630.

32 Wang Q, Xiao L, Liu X, *et al.* Special Z-scheme $Cu_3P/TiO_2$ hetero-junction for efficient photocatalytic hydrogen evolution from water. *J Alloys Compd* 2022; **894**: 162331.

33 Li J, Ma L, Fu C, *et al.* Urchinlike carbon-coated $TiO_2$ microspheres with enhanced photothermal-photocatalytic hydrogen evolution performance for full-spectrum solar energy conversion. *Ind Eng Chem Res* 2022; **61**: 6436–6447.

34 Bu Y, Chen Z, Li W. Using electrochemical methods to study the promotion mechanism of the photoelectric conversion performance of Ag-modified mesoporous g-$C_3N_4$ heterojunction material. *Appl Catal B-Environ* 2014; **144**: 622–630.

35 Kim H, Monllor-Satoca D, Kim W, *et al.* N-doped $TiO_2$ nanotubes coated with a thin $TaO_xN_y$ layer for photoelectrochemical water splitting: dual bulk and surface modification of photoanodes. *Energy Environ Sci* 2015; **8**: 247–257.

36 Liao J, Zhou J, Song Y, *et al.* Preselectable optical fingerprints of heterogeneous upconversion nanoparticles. *Nano Lett* 2021; **21**: 7659–7668.

37 Liao J, Zhou J, Song Y, *et al.* Optical fingerprint classification of single upconversion nanoparticles by deep learning. *J Phys Chem Lett* 2021; **12**: 10242–10248.

38 Guo X, Song W, Chen C, *et al.* Near-infrared photocatalysis of β-$NaYF_4$:$Yb^{3+}$,$Tm^{3+}$@ZnO composites. *Phys Chem Chem Phys* 2013; **15**: 14681–14688.

39 Bednarkiewicz A, Nyk M, Samoc M, *et al.* Up-conversion FRET from $Er^{3+}$/$Yb^{3+}$:$NaYF_4$ nanophosphor to CdSe quantum dots. *J Phys Chem C* 2010; **114**: 17535–17541.

40 Gao H, Yan S, Wang J, *et al.* Ion coordination significantly enhances the photocatalytic activity of graphitic-phase carbon nitride. *Dalton Trans* 2014; **43**: 8178–8183.

41 Bhunia MK, Abou-Hamad E, Anjum DH, *et al.* Solvent-free synthesis of quaternary metal sulfide nanoparticles derived from thiourea. *Part Part Syst Charact* 2018; **35**: 1700183.

42 Chen G, Ohulchanskyy TY, Kumar R, *et al.* Ultrasmall monodisperse $NaYF_4$:$Yb^{3+}$/$Tm^{3+}$ nanocrystals with enhanced near-infrared to near-infrared upconversion photoluminescence. *ACS Nano* 2010; **4**: 3163–3168.